In-Situ Nanoscale Focusing of Extreme Ultraviolet Solid-State High Harmonics

Aleksey Korobenko,[1] Sabaa Rashid,[2] Christian Heide,[3] Andrei Yu Naumov,[1] David A. Reis,[3] Pierre Berini,[2,4,5] Paul B. Corkum,[1] and Giulio Vampa[1,*]

[1]*Joint Attosecond Science Laboratory, National Research Council of Canada and University of Ottawa, Ottawa K1N 5A2, Canada*
[2]*Center for Research in Photonics, University of Ottawa, Ottawa K1N 6N5, Canada*
[3]*Stanford PULSE Institute, SLAC National Accelerator Laboratory, Menlo Park, California 94025, USA*
[4]*School of Electrical Engineering and Computer Science, University of Ottawa, Ottawa K1N 6N5, Canada*
[5]*Department of Physics, University of Ottawa, Ottawa K1N 6N5, Canada*

(Received 30 November 2021; revised 21 September 2022; accepted 1 December 2022; published 28 December 2022)

Extreme ultraviolet light delivering radiation with a wavelength shorter than approximately 100 nm is now available from solid-state sources. However, despite exceptional progress, efficient focusing of extreme ultraviolet photons to their ultimate diffraction limit remains a formidable challenge because of the precision of the focusing by curved, optical surfaces. Here we integrate coherent short-wavelength high-order harmonics from a MgO crystal, with a high-numerical-aperture, nanostructured, focusing element etched onto the surface of the crystal itself. We focus extreme ultraviolet light, seventh harmonic of an 800-nm laser, with a zone plate of numerical aperture 0.35, down to a waist radius of 150 nm, with 18% focusing efficiency. The estimated intensity approaches 10^7 W/cm^2. Future developments may demonstrate nanoscale laser ablation and miniaturization of extreme ultraviolet coherent sources on a chip.

DOI: 10.1103/PhysRevX.12.041036 Subject Areas: Condensed Matter Physics, Optics

I. INTRODUCTION

Modern electronics has developed tools for writing structures in solids at a spatial scale of 10 nm. With billions of dollars invested, it is the pinnacle of 21st century engineering. All technology, including photonics, heavily relies on the chip-scale integration enabled by nanoscale patterning. In this paper, we emphasize the convergence of extreme photonics, the generation and control of coherent extreme ultraviolet beams, and solid-state engineering, thereby opening the opportunity for integrated attosecond technology with structure and materials patterned on the nanoscale.

Seeded by the first demonstration of high-harmonic emission from a semiconducting crystal [1], nanostructured semiconducting surfaces have already demonstrated enhanced high-harmonic emission efficiency [2–6] and *in-situ* focusing [4,7] of visible and ultraviolet high harmonics. In addition, silicon can emit high harmonics [4], as do metals [8], both of which form the backbone of modern electronics. The tool set and the materials required for developing integrated extreme photonics are ready and will benefit other laser-based methods such as for the generation of shaped plasma harmonics. Clearly, two major trends of modern science are converging.

In the following, we review and extend our research on patterning magnesium oxide (MgO) [9], a dielectric crystal that emits extreme ultraviolet (XUV) harmonics up to 20 eV of photon energy, or 60-nm wavelength [10]. We pattern Fresnel zone plates with numerical aperture of up to 0.35 on the MgO surface, thereby combining generation and focusing of a high harmonic with wavelength of 114 nm (10.8-eV photon energy, overlapping with the vacuum ultraviolet spectral region) down to 150-nm focus.

Our demonstration of chip-scale generation and focusing of XUV light lays the foundation for developing a versatile and miniaturized platform to shape and control short-wavelength radiation. In so doing, we extend the use of nanostructured surfaces to a regime of solid-laser interactions dominated by dielectric crystals, which are significantly harder to structure than semiconductors (the latter class of materials emitting only visible harmonics [1]).

The manuscript is organized as follows. In Sec. II, we describe the experimental setup and the fabricated MgO surfaces. In Sec. III, we present and discuss the results, and in Sec. IV, we draw conclusions.

II. EXPERIMENTAL SETUP

Using the procedure detailed in the Appendix, we etch a set of Fresnel zone plates, 60 nm deep, on the surface of a

*gvampa@uottawa.ca

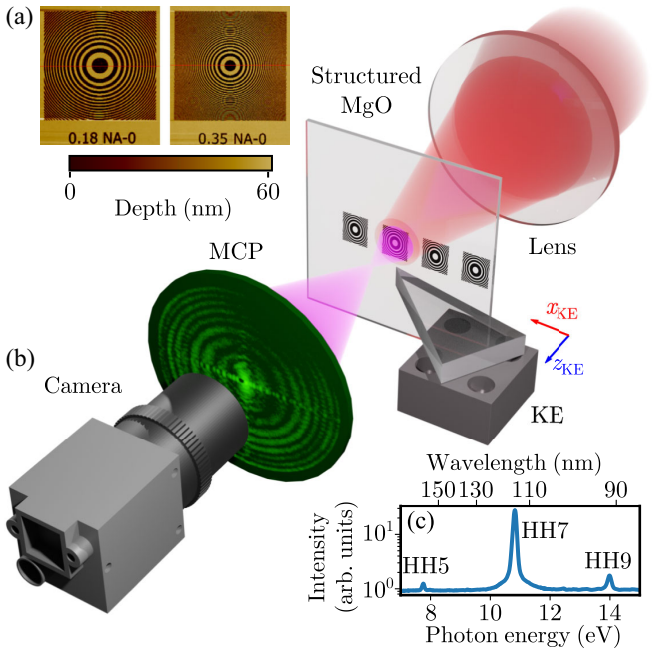

FIG. 1. (a) Atomic-force-microscope images of the two zone plates utilized in this study. They consist of rings etched in the MgO surface. Color scale represents surface depth. (b) The beam of an 800-nm laser is focused with a spherical lens onto a MgO crystal, with zone-plate patterns etched on its exit surface. The emitted high-harmonic radiation is captured on an imaging microchannel plate detector (MCP) equipped with a phosphor screen. The XUV yield is measured either as an electrical current on the MCP or as light flashes on the phosphor screen, imaged with a CCD camera. The shard of glass that acts as knife edge is mounted on a 2D nanopositioner (Micronix PPS20, 2-nm resolution) near the zone plate's focus. The knife edge (KE) can be moved normal to (axis z) and along (axis x) the sample surface. (c) High-harmonic spectrum emitted by the MgO surface and measured with a conventional XUV spectrometer consisting of a flat-field grating and MCP detector. The spectrum is dominated by the seventh harmonic (114-nm wavelength).

100-μm-thick, (100)-cut MgO single crystal. The results we present are obtained from 30×30 μm^2 zone plates, with focal lengths of 80 μm (NA 0.18) and 40 μm (NA 0.35) for 114-nm-wavelength radiation. The structures are characterized with atomic-force-microscope imaging, and the results are shown in Fig. 1(a).

A sketch of the experimental setup is shown in Fig. 1(b). The sample is mounted inside the vacuum chamber on a 3D linear stage. The output of a Ti:sapphire amplifier (Coherent Legend, 1-kHz repetition rate, 50-fs pulses) is attenuated to a pulse energy of approximately 10 μJ and focused with a fused silica lens to a Gaussian waist radius of $w_{\mathrm{fund}} = 60$ μm onto the structures, entering the crystal through the nonstructured surface first. Using a peak field intensity of approximately 3.7 TW/cm^2 allows us to minimize the laser propagation effects in the sample, keeping nonlinear phase variation across the fundamental beam profile below π [11]. The polarization is linear and horizontal. XUV radiation generated on the surface is collected on a 40-mm-diameter, round microchannel plate detector (MCP) with a phosphor screen, placed 100 mm away from the crystal. The observed XUV spectrum consists mostly of the seventh harmonic (114 nm), with higher harmonics not being generated, and the lower ones rejected by the MCP sensitivity curve [Fig. 1(c)].

We use two different approaches to quantify emitted XUV radiation. In the first approach, well suited for low intensities, the positions of individual photon hits are detected and binned at 500-Hz repetition rate with an external CCD camera imaging the phosphor screen of the detector assembly. This counting mode allows the diffracted XUV profile to be imaged with a very high dynamic range, but the photon hits per frame must be sparse enough to avoid pileup. In the second approach, we measure a transient current in the high-voltage circuit of the MCP power supply with a boxcar amplifier in sync with the laser pulses. This analog method allows for quicker measurement at the expense of losing spatial information.

Next to the structured surface, we mount a shard of a shattered fused silica microscope cover slip, 120 μm thick. The purpose of the shard is to block XUV light when it is inserted in the beam, thus allowing one-dimensional measurement of the XUV beam size. When mounted as shown in Fig. 1(b), the shard exposes a sharp apex with straight and smooth edges to the XUV beam generated on MgO. The quality of the edge is verified with an optical microscope. This geometry allows the shard to approach the surface to within tens of micrometers, with the apex serving as a knife edge (KE), and avoid clipping of a diverging beam with its back side.

III. RESULTS

Illuminating the structures with the intense infrared laser, we observe on the detector strong diffraction of the generated high-harmonic beam [Fig. 2(a)]. The diffraction pattern comprises a series of concentric rings and a bright center spot. The rings are consistent with diffraction from the circular pattern of the Fresnel zone plate, and we attribute the center spot to undiffracted (zeroth-order) radiation.

Having confirmed that the structured surface shapes the diffracted XUV beam, we now turn to measuring the focus. Figures 2(b) and 2(c) show the spatially integrated XUV flux as a function of the knife-edge position for a Fresnel zone plate having NA of 0.18 and 0.35, respectively. Fits to the data of a cumulative Gaussian distribution function yield waist radii ($1/e^2$) of (218 ± 15) and (150 ± 20) nm for the two zone plates, respectively (purple lines). Experimental constraints prevent us from measuring the perpendicular dimension. Despite the cylindrical symmetry of the zone plates, the use of linearly polarized light may induce slight asymmetry in the focus, which is not captured

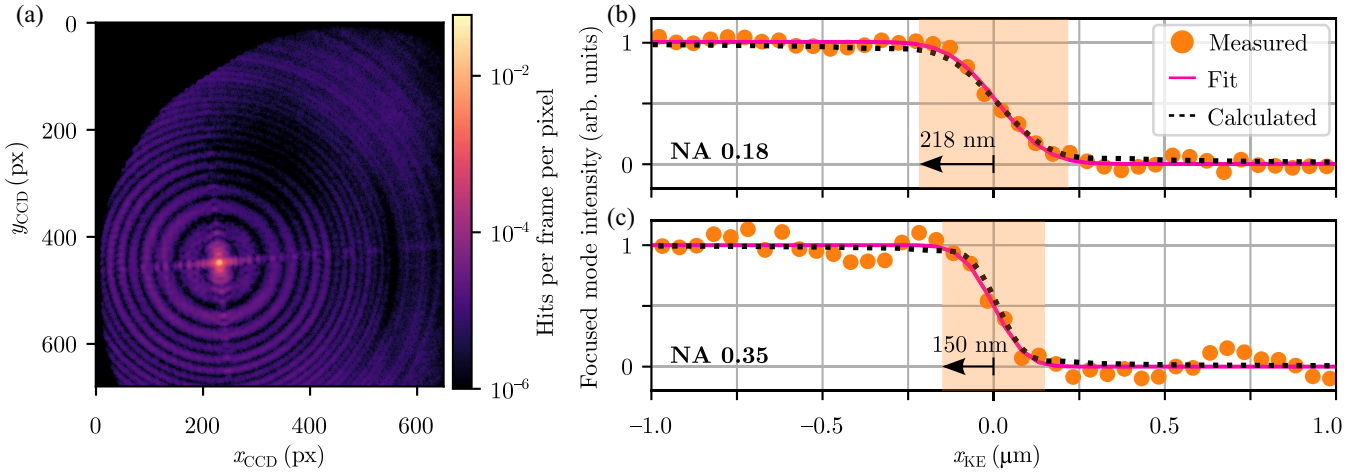

FIG. 2. (a) Diffraction of XUV light from the 0.35-NA Fresnel zone plate imaged by the phosphor screen. One pixel corresponds to about 40-μm size. (b),(c) Scan of the knife edge across the XUV focus for the 0.18-NA (b) and 0.35-NA (c) zone plates. Slowly varying contribution of the unfocused mode is subtracted. The solid purple line is a fit of a cumulative Gaussian distribution function to the data, with waist radius ($1/e^2$) as the only fit parameter. The dashed black line is the theoretical expectation obtained by simulating the knife-edge scan across a two-dimensional beam profile at the zone plate's focal plate. The focused beam profile is calculated by propagating the expected XUV distribution on the MgO surface to the focus with the angular spread method.

by our one-dimensional scan. Irradiating the plate with radially or azimuthally polarized light ensures that the illumination is also cylindrical symmetric, with the former polarization potentially producing a smaller focus [12].

Albeit challenging to manufacture and costly, external focusing elements for XUV light with high numerical apertures do exist (Fresnel zone plates [13], ellipsoidal mirrors [14], and Schwarzschild objectives [15]). At larger scales, the gargantuan EUV lithography tools are being upgraded to 0.55 numerical aperture. These remarkable advances are, however, incompatible with miniaturization, the focus of our work.

The simulations (black dashed lines) yield theoretical radii of 229 nm for the 0.18-NA plate and 121 nm for the 0.35-NA plate, in agreement with the measured values. Our simulations are based on the angular-spread method, which consists of (i) expanding the complex field distribution at the plane of the sample into a plane-wave basis, (ii) propagating each component to the focal plane imparting it with a phase **kf**, and (iii) summing all components.

Scanning the knife edge across the focus at various distances from the plates (z_{KE}) allows us to characterize the depth of focus (Rayleigh range). Figure 3(a) shows knife-edge scans at various z_{KE} positions for the 0.35-NA zone plate. The best-fit waist radii are reported in Fig. 3(b), from which the estimated Rayleigh range is 500 nm.

To estimate the focused power, we scan the knife edge at the focus over a wider distance; see Fig. 4. The slow decrease over approximately 32 μm corresponds to undiffracted light and higher-order foci. It is interrupted by a sharp drop of 18% corresponding to the first-order focus shown in Fig. 2(b). Since the detected harmonic spectrum essentially consists of only the seventh harmonic [see Fig. 1(c)], 18% of the total XUV power is contained in the nanofocus. This focusing efficiency is consistent with our simulations, as well as reported literature efficiencies for Fresnel zone plates [16].

Together with the measured waist, the focusing efficiency and the spatially integrated photon counts (accounting for 5% quantum efficiency of the MCP at 114 nm), we estimate that the XUV reaches a fluence of about 0.2 μJ/cm^2 at the focus of the 0.35-NA zone plate. Assuming a 50-fs-long XUV pulse, we estimate the peak intensity in the focus to be 4 MW/cm^2. Irradiating the zone plates with an infrared intensity closer to the damage threshold of the zone plates (10 TW/cm^2) increases the

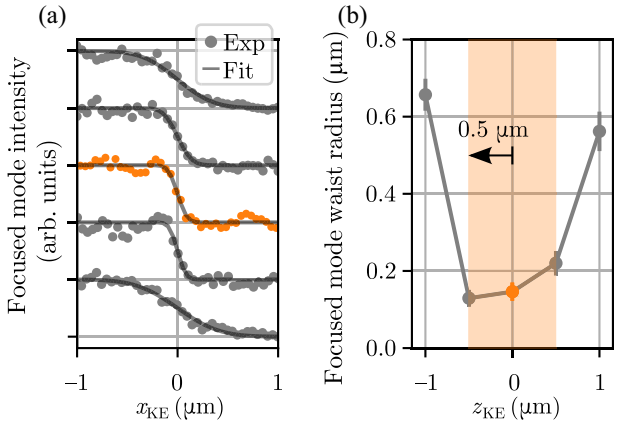

FIG. 3. (a) Knife-edge scans at various distances from the 0.35-NA zone plate relative to the focus position ($z_{KE} = 0$). (b) Fitted XUV waist radius as a function of z_{KE}. The Rayleigh range is estimated to be 0.5 μm.

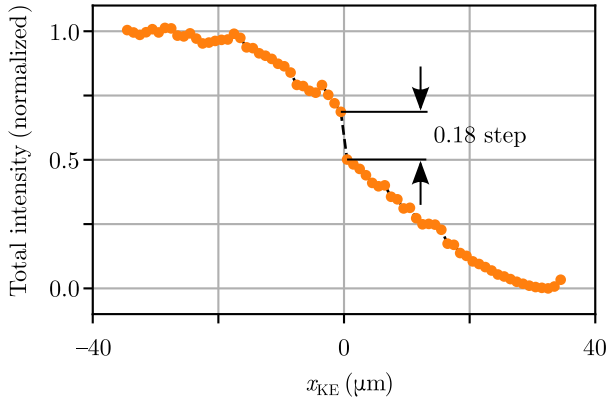

FIG. 4. Knife-edge scan of the 0.18-NA zone plate over a wider range that examines all undiffracted light as well as higher-order foci. The slow drop corresponds to a 32-μm XUV beam, while the sharp drop in the middle corresponds to the first-order focus [a finer scan in this region is reported in Fig. 2(b)]. The focused XUV contains 18% of the total emitted photons.

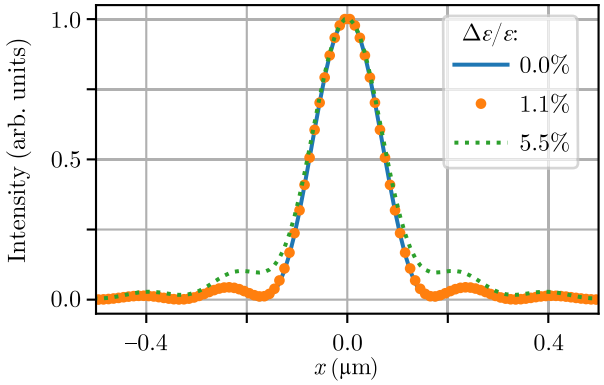

FIG. 5. Simulated nanofocus for various relative spectral bandwidths. Blue line, monochromatic light at the seventh harmonic; orange circles, a Gaussian spectrum about the center wavelength with 1.1% relative energy half-spread ($1/e^2$). This bandwidth corresponds to that measured experimentally. Green dots: a fivefold increase of bandwidth results in a modest 10% widening of the focus.

diffracted XUV energy measured as photon hits on the detector without the knife edge, to 3 fJ/pulse. Assuming that the first order of diffraction contains the theoretical 30% of the total diffracted signal (i.e. all signal, excluding the 0th order mode), we estimate a maximum fluence of 2 μJ/cm^2, or an intensity of 40 MW/cm^2, a tenfold increase.

The current XUV fluence is particularly suited for two-color ablation [17]. In two-color ablation, the XUV beam creates a nanoscopic volume of free electrons that a moderately intense infrared field, either from a secondary beam or from the undiffracted zeroth order of the zone plate, avalanches to the critical density for ablation [17], approximately 10^{19} cm^{-3} for absorption of 40-eV photons in a 10-nm depth [18]. The current maximum fluence should generate 10^{18}-cm^{-3} electrons (10-eV photons absorbed in 10-nm depth). Multiplication of this seed density by a factor of 10 through the avalanche is possible.

Higher XUV intensity will aid the avalanche. The most promising approach to increase the flux is to increase the infrared intensity (I_0), which can be achieved by shortening the driving pulse duration or using a longer wave-length driver [10]. MgO can sustain irradiation at 25 TW/cm^2 with 7-fs pulses [19]. Reaching XUV intensities of approximately 10 GW/cm^2 would be sufficient to evaporate polymers [18] and biological tissue and even to drive nonlinearities in materials [20–22]. As we demonstrate below, the increased harmonic bandwidth (approximately 6% relative bandwidth) ensuing from the shorter driving pulse is compatible with our current zone plates.

Controlling ablation requires attenuating the strong infrared driver that contaminates the focus. This can be done by illuminating zone plates designed to operate in reflection, rather than in transmission, at the Brewster angle for the infrared beam, where reflectivity vanishes. A slight rotation of the infrared polarization away from the reflection plane can add a controlled amount of infrared field for ablation without affecting the XUV focus [23].

Although diffractive optical elements are inherently chromatic, the good agreement between the measured foci and the ones calculated for a single high-harmonic wavelength of 114 nm suggest that chromatic aberrations are negligible in our experimental conditions. To confirm this expectation, Fig. 5 compares the foci calculated at the center wavelength (blue line) and over the bandwidth of the seventh harmonic ($\Delta\varepsilon/\varepsilon = 1.1\%$ FWHM, orange line), for the 0.35-NA zone plate. No chromatic aberration is visible. In fact, we can even afford a fivefold increase of bandwidth and enlarge the focus by a mere 10% (green dots in Fig. 5).

Alongside spatial aberration is temporal broadening at the focus. Temporal broadening arises because the pulses converging from the outer zones travel a longer distance than the center ones. Given that each zone induces a full-wavelength delay, we expect a pulse lengthening of 4.5 and 9 fs for the 0.18- and 0.35-NA plates, respectively. Both are smaller than the driving pulse duration.

This tolerance to chromatic and temporal distortions is due to the small plate size, which translates to a modest number of zones. The plate size is matched to the infrared focus waist, which is typically tens of microns to reach the required intensity to trigger XUV emission. This match is another advantage of our *in-situ* approach, over using large external zone plates [13].

The grating pattern that defines the zone plates is designed to shape the driving infrared field by inducing a phase delay of $\pi/7$ between adjacent grooves when measured at the top (exit) surface to control high-harmonic emission. This delay translates into a half-wave delay at the seventh harmonic, which is expected to lead to the

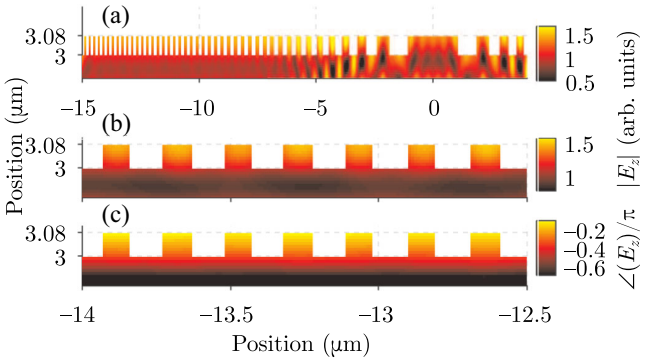

FIG. 6. Two-dimensional finite-difference simulation (in the frequency domain) of an infrared driver propagating to a 0.35-NA zone plate etched in the MgO surface from the MgO substrate (bottom to top). (a),(b) Amplitude of electric field (polarized out of plane) across half of the zone plate (a), and in a smaller region near the edge (b). (c) Phase of infrared field across the same region as in (b). Amplitude and phase modulation varies across the plate.

strongest focusing. To verify this assumption, we perform finite-difference simulations [24,25] of the infrared driver propagating through the MgO crystal. Figure 6 shows two-dimensional images of the field magnitude [Figs. 6(a) and 6(b)] and phase [Fig. 6(c)] distribution at the structured surface of a 0.35-NA zone plate, 80 nm deep. Clearly, a significant amplitude modulation is also present alongside a phase modulation. These modulations arise from the variation of the grating pitch across the structure, which goes from micron scale in the middle, to deep subwavelength toward the edge. As a result, scattering of the infrared field varies across the structure. In other words, the zone plates become progressively a metasurface [26] as the feature size becomes subwavelength. Although the zone plates seem to operate in a more complicated fashion than expected, the added complexity provides the opportunity to control amplitude and phase of the infrared driver (and, consequently, of the harmonics) by borrowing concepts and methodologies developed for metasurfaces. For example, computer-assisted, or inverse, design [27] can be employed to explore nonintuitive patterns that would achieve a desired XUV focus by acting upon the infrared driver, or to smooth out the field hot spots that may be responsible for the approximately 10% lower damage threshold of the structured surface compared to bulk. Inverse design has not yet been applied to high-field nonlinearities.

IV. CONCLUSIONS

We demonstrate highly efficient *in-situ* focusing of 11-eV photons down to a waist radius of 150 nm with numerical apertures of up to 0.35, an achievement that competes with the best *ex-situ* focusing elements for XUV radiation, such as ellipsoidal mirrors, Schwarzschild objectives, and Fresnel zone plates. We estimate the intensity at the focus to be approximately 40 MW/cm^2. We expect the unique combination of short wavelength, small focus, and high intensity to enable many applications, such as direct laser nanostructuring and nonlinear imaging with chemical specificity, an extension to the element-specific imaging pioneered at higher photon energies [20,21], and photoelectron spectronanoscopy [28].

Ablating materials will not even need a stronger XUV beam [17,18]: ablation can be induced by a moderately intense near-infrared pulse starting from a nanoscale volume of seed electrons created by the XUV beam. In fact, in several attosecond techniques an infrared pulse is added to the XUV pulse in order to produce the nonlinearity that allows attosecond measurements. The infrared is there in streaking [29], RABBIT [30], and transient absorption [31] to name a few prominent examples. *In-situ* focusing will add to this *modus operandi* of attosecond technology, allowing attosecond experiments with nanometer spatial resolution.

Finally, our demonstration of a functional nanostructured dielectric surface for control of XUV radiation paves the way for integrating short-wavelength sources and attosecond experiments on a chip.

ACKNOWLEDGMENTS

We thank Dave Crane and Ryan Kroeker for providing continuing technical support. G. V., C. H., and D. A. R. acknowledge funding from the W. M. Keck Foundation. C. H. acknowledges support from the Alexander von Humboldt foundation. G. V., A. K., and P. B. C. acknowledge support from the Joint Center for Extreme Photonics. P. B. C. acknowledges funds from the U.S. Defense Threat Reduction (Grant No. 1-19-1-0026) and from the U.S. Air Force Office of Scientific Research (Grant No. FA9550-16-1-0109). P. B. acknowledges funding from the Natural Sciences and Engineering Research Council of Canada.

APPENDIX: FABRICATION

The fabrication procedure is an evolution of that presented in Ref. [9]. A 100-μm-thick (100)-oriented MgO substrate (CRYSTAL GmbH) is dehydration baked at 200 °C on a hot plate for an hour, then exposed to Ar-reactive-ion etching [(RIE), SAMCO 10NR system] for 2 min at an applied rf power of 25 W, Ar flow rate of 10 sccm, and a chamber pressure of 3 Pa to remove surface contaminants. Polymethylmethacrylate (PMMA) resist (950k MW, 2 wt % in anisole, Kayaku Advanced Materials) is spin coated immediately on the MgO substrate to a thickness of 70 nm (Laurell WS-650-23NPP spin coater), then baked at 200 °C for 2 h. ESPACER 300Z (SHOWA DENKO) is then spin coated on the substrate to dissipate charging. The zone plates are patterned from bitmap files by exposing PMMA with the helium ion microscope [(HIM), Orion NanoFab, Zeiss; Nano

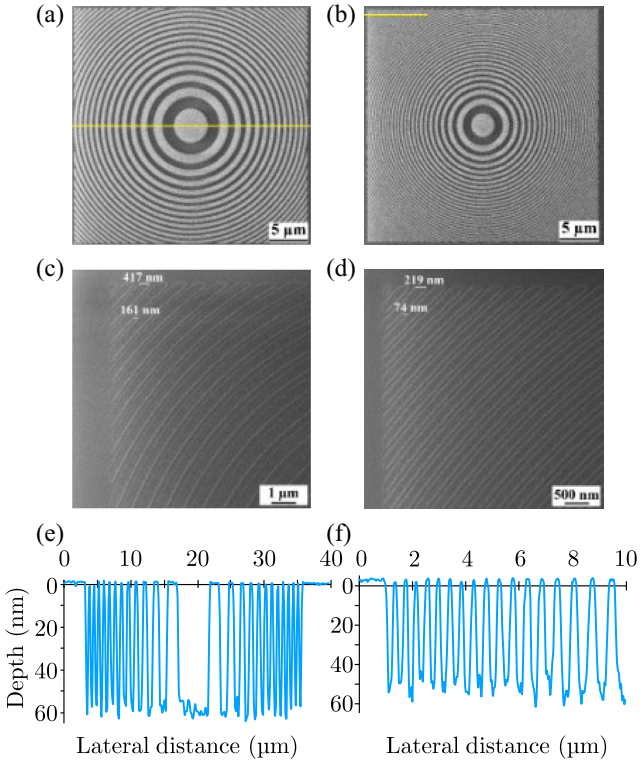

FIG. 7. (a),(b) HIM images taken with an electron flood gun of 30×30 μm^2 zone plates of 0.18 and 0.35 NA, respectively, etched into MgO. (c),(d) High-magnification HIM images acquired at the top left corner of the 0.18- and 0.35-NA zone plates, respectively, with measured features labeled in white. (e) AFM linescan through the middle of the 0.18-NA zone plate [yellow trace in (a)] showing a depth of 60 nm. (f) AFM line scan of the top left corner of the 0.35-NA zone plate where the structures are densest [yellow trace in (b)], showing an etch depth of 60 nm for both. These structures are transferred from a PMMA mask by wet etching in 10% (v/v) H_3PO_4 in IPA.

Patterning and Visualization Engine, Fibics)] [32]. A helium beam current of 0.5 pA is used to pattern the 0.18- and 0.35-NA zone plates at a landing energy of 25 kV to deliver a dose of 8 μC/cm^2 with a beam step size of 20 nm, and a dwell time of 64 μs. Postexposure, the substrate is submerged in a deionized (DI) water bath for 10 s to remove ESPACER 300Z, rinsed with DI water, and dried with nitrogen. Exposed PMMA is then developed in a mixture of methyl isobutyl ketone (MIBK):isopropanol (IPA) in a ratio of 1∶3 for 2 min at 20 °C, followed by a 30-s bath in IPA. A step height of 60 nm is then etched into the MgO by submerging the substrate in a 10% (v/v) H_3PO_4 in IPA for 70 s. The etching is performed at room temperature in an ultrasonic bath at 80 kHz and 30% power. The substrate is then submerged in acetone for 2 min to remove the PMMA mask, followed by another 30 s in an IPA bath. We change the solvent of the etching solution from water to IPA to mitigate delamination of the PMMA film from the MgO surface (catastrophic delamination of PMMA from MgO is observed when etching the zone plates in a water-based-etching solution). Since MgO is hygroscopic, we minimize exposure of the substrate to water when ESPACER 300Z is removed and during wet etching. Agitation during etching accelerates the etching rate and results in anisotropic etching. Previous literature demonstrated the use of an organic-based solvent to etch MgO in an agitated solution and compared it to a water-based solvent and stagnant etching [33].

AFM scans (not shown) reveal that a thin (approximately 10 nm) layer of hardened PMMA remains behind post-removal of PMMA. Therefore, an O_2 RIE is used to remove the residue (5 min at an applied rf power of 25 W, O_2 flow rate of 10 sccm, and chamber pressure of 3 Pa). However, removal of the residue significantly reduces the HIM imaging contrast. Thus, we develop a sequence of steps to characterize the fabricated structures with HIM before removal of the residue pre-O_2 RIE, and subsequently, with AFM after removal of the residue (post-O_2 RIE).

A HIM equipped with an electron flood gun to facilitate imaging of insulating substrates is used to characterize the etched zone plates pre-O_2 RIE [Fig. 7(a)–7(d)]. Figures 7(a) and 7(b) show the fabricated 30×30 μm^2 zone plates of 0.18 and 0.35 NA, respectively. Figures 7(c) and 7(d) show high-magnification images taken at the top left corner of the 0.18- and 0.35-NA zone plates, respectively, with measurement dimensions labeled in white. Figures 7(e) and 7(f) show AFM (Park Systems NX10) line scans of the depth profile obtained through the middle of the 0.18-NA zone plate [yellow trace on Fig. 7(a)] and at the top left corner of the 0.35-NA zone plate [yellow trace on Fig. 7(b)], respectively, where the structures are densest. Both profiles show the same depth of 60 nm etched in MgO post-O_2 RIE.

[1] S. Ghimire and D. A. Reis, *High-Harmonic Generation from Solids*, Nat. Phys. **15**, 10 (2019).
[2] S. Han, H. Kim, Y. W. Kim, Y.-J. Kim, S. Kim, I.-Y. Park, and S.-W. Kim, *High-Harmonic Generation by Field Enhanced Femtosecond Pulses in Metal-Sapphire Nanostructure*, Nat. Commun. **7**, 13105 (2016).
[3] G. Vampa, B. Ghamsari, S. S. Mousavi, T. Hammond, A. Olivieri, E. Lisicka-Skrek, A. Y. Naumov, D. Villeneuve, A. Staudte, P. Berini *et al.*, *Plasmon-Enhanced High-Harmonic Generation from Silicon*, Nat. Phys. **13**, 659 (2017).
[4] M. Sivis, M. Taucer, G. Vampa, K. Johnston, A. Staudte, A. Y. Naumov, D. Villeneuve, C. Ropers, and P. Corkum, *Tailored Semiconductors for High-Harmonic Optoelectronics*, Science **357**, 303 (2017).
[5] H. Liu, C. Guo, G. Vampa, J. L. Zhang, T. Sarmiento, M. Xiao, P. H. Bucksbaum, J. Vučković, S. Fan, and D. A. Reis, *Enhanced High-Harmonic Generation from an All-Dielectric Metasurface*, Nat. Phys. **14**, 1006 (2018).
[6] H. Liu, G. Vampa, J. L. Zhang, Y. Shi, S. Buddhiraju, S. Fan, J. Vuckovic, P. H. Bucksbaum, and D. A. Reis, *Beating*

Absorption in Solid-State High Harmonics, Commun. Phys. **3**, 192 (2020).

[7] D. Gauthier, S. Kaassamani, D. Franz, R. Nicolas, J.-T. Gomes, L. Lavoute, D. Gaponov, S. Février, G. Jargot, M. Hanna, W. Boutu, and H. Merdji, *Orbital Angular Momentum from Semiconductor High-Order Harmonics*, Opt. Lett. **44**, 546 (2019).

[8] A. Korobenko, S. Saha, A. T. Godfrey, M. Gertsvolf, A. Y. Naumov, D. M. Villeneuve, A. Boltasseva, V. M. Shalaev, and P. B. Corkum, *High-Harmonic Generation in Metallic Titanium Nitride*, Nat. Commun. **12**, 4981 (2021).

[9] A. Korobenko, S. Rashid, C. Heide, A. Y. Naumov, D. Reis, P. Berini, P. Corkum, and G. Vampa, *Generation of Structured Coherent Extreme Ultraviolet Beams from an* MgO *Crystal*, Opt. Express **29**, 24161 (2021).

[10] Y. S. You, D. A. Reis, and S. Ghimire, *Anisotropic High-Harmonic Generation in Bulk Crystals*, Nat. Phys. **13**, 345 (2017).

[11] R. Adair, L. L. Chase, and S. A. Payne, *Nonlinear Refractive Index of Optical Crystals*, Phys. Rev. B **39**, 3337 (1989).

[12] R. Dorn, S. Quabis, and G. Leuchs, *Sharper Focus for a Radially Polarized Light Beam*, Phys. Rev. Lett. **91**, 233901 (2003).

[13] M. Wieland, C. Spielmann, U. Kleineberg, T. Westerwalbesloh, U. Heinzmann, and T. Wilhein, *Toward Time-Resolved Soft X-Ray Microscopy Using Pulsed fs-High-Harmonic Radiation*, Ultramicroscopy **102**, 93 (2005).

[14] H. Motoyama, A. Iwasaki, Y. Takei, T. Kume, S. Egawa, T. Sato, K. Yamanouchi, and H. Mimura, *Broadband Nano-Focusing of High-Order Harmonics in Soft X-Ray Region with Ellipsoidal Mirror*, Appl. Phys. Lett. **114**, 241102 (2019).

[15] M. Toyoda, K. Yamasoe, A. Tokimasa, K. Uchida, T. Harada, T. Terasawa, T. Amano, T. Watanabe, M. Yanagihara, and H. Kinoshita, *Demonstrating 30-nm Spatial Resolution of Three-Multilayer-Mirror Objective for Extreme Ultraviolet Microscopy: Imaging Test by Observing Lithography Mask*, Appl. Phys. Express **7**, 102502 (2014).

[16] J. Kirz, *Phase Zone Plates for X Rays and the Extreme UV*, J. Opt. Soc. Am. **64**, 301 (1974).

[17] X. Yu, Z. Chang, P. Corkum, and S. Lei, *Fabricating Nanostructures on Fused Silica Using Femtosecond Infrared Pulses Combined with Sub-Nanojoule Ultraviolet Pulses*, Opt. Lett. **39**, 5638 (2014).

[18] K. Sakaue, H. Motoyama, R. Hayashi, A. Iwasaki, H. Mimura, K. Yamanouchi, T. Shibuya, M. Ishino, T.-H. Dinh, H. Ogawa *et al.*, *Surface Processing of PMMA and Metal Nano-Particle Resist by Sub-Micrometer Focusing of Coherent Extreme Ultraviolet High-Order Harmonics Pulses*, Opt. Lett. **45**, 2926 (2020).

[19] A. Korobenko, T. Hammond, C. Zhang, A. Y. Naumov, D. Villeneuve, and P. Corkum, *High-Harmonic Generation in Solids Driven by Counter-Propagating Pulses*, Opt. Express **27**, 32630 (2019).

[20] T. Helk, E. Berger, S. Jamnuch, L. Hoffmann, A. Kabacinski, J. Gautier, F. Tissandier, J.-P. Goddet, H.-T. Chang, J. Oh *et al.*, *Table-Top Extreme Ultraviolet Second Harmonic Generation*, Sci. Adv. **7**, eabe2265 (2021).

[21] R. K. Lam, S. Raj, T. Pascal, C. Pemmaraju, L. Foglia, A. Simoncig, N. Fabris, P. Miotti, C. Hull, A. Rizzuto *et al.*, *Soft X-Ray Second Harmonic Generation as an Interfacial Probe*, Phys. Rev. Lett. **120**, 023901 (2018).

[22] H. Rottke, R. Y. Engel, D. Schick, J. O. Schunck, P. S. Miedema, M. C. Borchert, M. Kuhlmann, N. Ekanayake, S. Dziarzhytski, G. Brenner *et al.*, *Probing Electron and Hole Colocalization by Resonant Four-Wave Mixing Spectroscopy in the Extreme Ultraviolet*, Sci. Adv. **8**, eabn5127 (2022).

[23] G. Vampa, Y. You, H. Liu, S. Ghimire, and D. Reis, *Observation of Backward High-Harmonic Emission from Solids*, Opt. Express **26**, 12210 (2018).

[24] N. J. Champagne II, J. G. Berryman, and H. M. Buettner, *FDFD: A 3D Finite-Difference Frequency-Domain Code for Electromagnetic Induction Tomography*, J. Comput. Phys. **170**, 830 (2001).

[25] Y. Shi, W. Shin, and S. Fan, *Multi-Frequency Finite-Difference Frequency-Domain Algorithm for Active Nanophotonic Device Simulations*, Optica **3**, 1256 (2016).

[26] N. Yu and F. Capasso, *Flat Optics with Designer Metasurfaces*, Nat. Mater. **13**, 139 (2014).

[27] S. Molesky, Z. Lin, A. Y. Piggott, W. Jin, J. Vucković, and A. W. Rodriguez, *Inverse Design in Nanophotonics*, Nat. Photonics **12**, 659 (2018).

[28] A. Mikkelsen, J. Schwenke, T. Fordell, G. Luo, K. Klünder, E. Hilner, N. Anttu, A. Zakharov, E. Lundgren, J. Mauritsson *et al.*, *Photoemission Electron Microscopy Using Extreme Ultraviolet Attosecond Pulse Trains*, Rev. Sci. Instrum. **80**, 123703 (2009).

[29] J. Itatani, F. Quéré, G. L. Yudin, M. Y. Ivanov, F. Krausz, and P. B. Corkum, *Attosecond Streak Camera*, Phys. Rev. Lett. **88**, 173903 (2002).

[30] P.-M. Paul, E. S. Toma, P. Breger, G. Mullot, F. Augé, P. Balcou, H. G. Muller, and P. Agostini, *Observation of a Train of Attosecond Pulses from High Harmonic Generation*, Science **292**, 1689 (2001).

[31] M. Schultze, K. Ramasesha, C. Pemmaraju, S. Sato, D. Whitmore, A. Gandman, J. S. Prell, L. Borja, D. Prendergast, K. Yabana *et al.*, *Attosecond Band-Gap Dynamics in Silicon*, Science **346**, 1348 (2014).

[32] S. Rashid, J. Walia, H. Northfield, C. Hahn, A. Olivieri, A. C. Lesina, F. Variola, A. Weck, L. Ramunno, and P. Berini, *Helium Ion Beam Lithography and Liftoff*, Nano Futures **5**, 025003 (2021).

[33] C. Alain, L. N. Phong, and I. Shih, MgO *Micromachining for Superconductor Focal Plane Arrays*, in *Infrared Technology and Applications XXIII, Orlando, FL* (International Society for Optics and Photonics, 1997), Vol. 3061, pp. 974–982.